Received: 11 September 2019 | Revised: 30 March 2020 | Accepted: 3 April 2020

DOI: 10.1002/eom2.12024

RESEARCH ARTICLE

EcoMat FUNCTIONAL MATERIALS FOR GREEN ENERGY AND ENVIRONMENT WILEY

Aggregation-induced emission luminogen: A new perspective in the photo-degradation of organic pollutants

Zhen Hu[1] | Ying Li[2] | Miaomiao Kang[2] | Md. Monarul Islam[1] | Mengsi Chen[1] | Jun Zhang[2] | Ye Xiao[1] | Xing Feng[1] | Carl Redshaw[3] | Menglong Zhang[4] | Qing Chen[5] | Sheng Xie[2] | Jacky W. Y. Lam[2] | Ben Zhong Tang[2]

[1]Guangdong Provincial Key Laboratory of Functional Soft Condensed Matter, School of Material and Energy, Guangdong University of Technology, Guangzhou, China

[2]Department of Chemistry, the Hong Kong Branch of Chinese National Engineering Research Center for Tissue Restoration and Reconstruction and Institute for Advanced Study, The Hong Kong University of Science and Technology Clear Water Bay, Hong Kong, China

[3]Department of Chemistry and Biochemistry, University of Hull, Hull, UK

[4]Institute of Semiconductors Materials and Technology, South China Normal University, Guangzhou, China

[5]Beijing Enterprise Water Group Limited, Beijing, China

Correspondence
Xing Feng, Guangdong Provincial Key Laboratory of Functional Soft Condensed Matter, School of Material and Energy, Guangdong University of Technology, Guangzhou 510006, China.
Email: hyxhn@sina.com

Menglong Zhang, Institute of Optoelectronic Materials and Technology, South China Normal University, Guangzhou 510631, China.
Email: mlzhang@m.scnu.edu.cn

Sheng Xie and Ben Zhong Tang, Department of Chemistry, the Hong Kong Branch of Chinese National Engineering Research Center for Tissue Restoration and Reconstruction and Institute for Advanced Study, The Hong Kong University of Science and Technology Clear Water Bay, Kowloon, Hong Kong, China.
Email: sheng.xie@ki.se, tangbenz@ust.hk

Abstract

Both the variety and uniqueness of organic semiconductors has contributed to the rapid development of environmental engineering applications and renewable fuel production, typified by the photodegradation of organic pollutants or water splitting. This paper presents a rare example of an aggregation-induced emission luminogen as a highly efficient photocatalyst for pollutant decomposition in an environmentally relevant application. Under irradiation, the tetraphenylethene-based AIEgen (**TPE-Ca**) exhibited high photo-degradation efficiency of up to 98.7% of Rhodamine B (RhB) in aqueous solution. The possible photocatalytic mechanism was studied by electron paramagnetic resonance and X-ray photoelectron spectroscopy spectra, electrochemistry, thermal imaging technology, ultra-performance liquid chromatography and high-definition mass spectrometry, as well as by density functional theory calculations. Among the many diverse AIEgens, this is the first AIEgen to be developed as a photocatalyst for the degradation of organic pollutants. This research will open up new avenues for AIEgens research, particularly for applications of environmental relevance.

Zhen Hu and Ying Li contributed equally to this work.

Funding information
AIEgen Biotech Co., Ltd.; Overseas Travel Grant, Grant/Award Number: EP/R023816/1; Talented Young Scientist Program (TYSP) Fellowship, Grant/Award Number: 402180111; Guangdong University of Technology, Grant/Award Number: 1108-220413205; Natural Science Foundation of Guangdong Province of China, Grant/Award Number: 2019A1515010925; National Natural Science Foundation of China, Grant/Award Numbers: 21602014, 51620105009, 21975054

KEYWORDS
aggregation-induced emission luminogen, photocatalysis mechanism, photodegradation, radical species

1 | INTRODUCTION

Increased energy consumption and environmental issues are becoming increasingly problematic as the global population grows and extensive industrialization continues at an ever-increasing pace.[1] Among them, water pollution is one of the most important environmental problems that mankind faces today.[2] To-date, much effort has been devoted to exploring more efficient technologies for both the prevention and control of water pollution, including the use of chemical and physical methods. Photocatalytic methods are one of the cutting-edge techniques available for water treatment because of mild operating conditions, high efficiency, and relatively low cost.[3]

Currently, numerous photocatalytically active materials including inorganic (TiO_2, ZnO, CdS, etc.),[4] metal-free (g-C_3N_4),[5] organometallic complexes,[6] and metal-nitrides (GaN/InGaN)[7] as well as metal-organic frameworks (MOFs)[8] have been extensively studied for pollutant decomposition due to their good stability, high catalytic activity, and favorable environmental characteristics. In the case of photocatalytically active materials, they can capture photons with suitable light energy, generate electrons and holes in the conduction and valence bands, respectively, which can react with water and oxygen to produce reactive oxygen species (ROS, such as hydroxyl radicals, superoxide, hydrogen peroxide and singlet oxygen), and further degrade organic dyes or produce hydrogen.[9]

The ability to generate the ROS is a key point in the use of photoactive materials.[10] Compared to the traditional photoactive materials mentioned above, organic semiconductor materials have attracted considerable attention as photocatalysts, due to their low costs and tunable energy gaps that are responsive to a wide-range of visible light, leading to highly efficient utilization of solar energy.[11] However, examples of photocatalysts are rare due to the aggregation-caused quenching (ACQ) effect, which leads to low efficiency of ROS generation.[12] On the other hand, the lack of catalytic reaction sites in many organic semiconductor materials lowers the photocatalytic efficiency. The heterogeneous structures of alkalinized-C_3N_4, TiO_2-based hybrid materials[13] can accelerate catalytic reactions by improving both the light harvesting ability and ROS generation efficiency via photo-generated electrons and holes.

In 2001, Tang's group developed a series of novel luminogens, defined as "aggregation-induced emission (AIE),"[12a-c] which exhibited an abnormal photo-physical phenomenon, *viz* weak or non-emissive in solution, but emitting bright light with high quantum yield (up to 100%) in the aggregate state. These high-performance AIEgens with their unique optical properties can be used for organic light-emitting diodes, fluorescence probes, as well as in cell imaging etc.[12] On the other hand, AIEgens with appropriate molecular structures in the aggregated state are favorable for the formation of highly ROS for photodynamic therapy (PDT).[14] Thus, if nascent ROS are involved in the photocatalytic reaction of organic pollutants in water, then the AIEgen would be regarded as an excellent candidate for potential clean environmental applications. Previously, Tang with coworker have demonstrated that a tailored cyanostilbene-based molecule with the AIE feature exhibited a controllable regio- and stereo-selective photodimerization or photocyclization reaction under UV irradiation with color-tuneable properties in aqueous medium via a radical process.[15] On the other hand, Zhao *et al*. reported that cyanopyridinium-based cationic salts exhibited an enhanced emission with remarkable structure-dependent singlet-oxygen generation ability under white light-illumination for photodynamic anticancer and antibacterial therapy.[16] Both examples indicated that cyanostilbene derivatives possess a typical AIE characteristic with ideal photo-sensitizers for ROS generation.[17]

To explore the suitability for employing AIEgens in environmental applications, this article presents a new application of AIEgens in the photodegradation of

organic pollution in aqueous solution. As an organic photocatalyst, photoactive AIEgen[17c] can play a significant role in the photodegradation of Rhodamine with high efficiency (98.7%); the whole process has been investigated by UV-vis spectroscopy, photoluminescence (PL), photo-electrochemistry, and ultra-performance liquid chromatography/high-definition mass spectrometry (UPLC/HDMS). More importantly, thermal imaging, electron paramagnetic resonance (EPR) spin-trap, X-ray photoelectron spectroscopic (XPS) techniques, and transmission electron microscopy (TEM) have been used to monitor the entire photocatalytic process and to probe a possible mechanism.

2 | EXPERIMENTAL SECTION

2.1 | Materials

Unless otherwise stated, all reagents were purchased from commercial sources and were used without further purification. Tetrahydrofuran was distilled immediately prior to use. Dulbecco-modified eagle medium (DMEM), fetal bovine serum (FBS), penicillin G (100 U mL^{-1}), streptomycin (100 U mL^{-1}), and 0.25% trypsin 0.53×10^{-3} M EDTA solution were obtained from Gibco. 3-(4,5-dimethylthiazol-2-yl)-2,5-diphenyltetrazolium bromide (MTT) was purchased from Sigma-Aldrich company.

2.2 | Synthesis

2.2.1 | Synthesis of (Z)-2-(4′-(9H-carbazol-9-yl)-[1,1′-biphenyl]-4-yl)-3-(4-(1,2,2-triphenylvinyl) phenyl) acrylonitrile (TPE-Ca)

4-(1,2,2-Triphenylvinyl)benzaldehyde (TPE-CHO) (627 mg, 1.74 mmol, 1.00 equiv), 2-(4′-(9H-carbazol-9-yl)-[1,1′-biphenyl]-4-yl)acetonitrile (**1**) (240 mg, 2.09 mmol, 1.20 equiv), and potassium *t*-butoxide (380 mg, 2.09 mmol, 1.20 equiv) were added into a 100 mL round-bottom flask under a nitrogen atmosphere. Then 30 mL of ethanol was added, and the mixture was refluxed overnight. After cooling to room temperature, the mixture was filtered and washed three times with ethanol. The residue was further crystallized in CH_2Cl_2 and hexane to give a yellow powder (327 mg, yield 70%). ^{1}H NMR (600 MHz, $CDCl_3$) δ 8.16 (d, J = 7.8 Hz, 2H), 7.85 (d, J = 8.4 Hz, 2H), 7.77 (q, J = 8.6 Hz, 4H), 7.69 (dd, J = 17.2, 8.3 Hz, 4H), 7.53-7.46 (m, 3H), 7.43 (dd, J = 11.3, 4.0 Hz, 2H), 7.31 (t, J = 7.4 Hz, 2H), 7.19-7.01 (m, 17H). ^{13}C NMR (151 MHz, $CDCl_3$) δ 146.6, 143.4, 143.3, 143.2, 142.4, 141.8, 140.95, 140.8, 140.0, 139.0, 137.4, 134.0, 132.0, 131.6, 131.4, 131.3, 131.3, 128.8, 128.4, 127.9, 127.9, 127.7, 127.7, 127.4, 126.9, 126.8, 126.7, 126.5, 126.0, 123.5, 120.4, 120.1, 118.1, 110.1, 109.8. high-resolution mass spectrometry (HRMS) FABS ($M + H^+$) calcd for $C_{53}H_{36}N_2$ 700.89, found 701.17.

2.3 | X-ray crystallography

Crystallographic data for the compound was collected on a Bruker APEX 2 CCD diffractometer with graphite monochromated Mo Kα radiation (λ = 0.71073 Å) in the ω scan mode. The structure was solved by charge flipping or direct methods algorithms and refined by full-matrix least-squares methods on F^2. All esds (except the esd in the dihedral angle between two l.s. planes) were estimated using the full covariance matrix. The cell esds were considered individually in the estimation of esds in distances, angles, and torsion angles. Correlations between esds in cell parameters were only used when they were defined by crystal symmetry. An approximate (isotropic) treatment of cell esds was used for estimating esds involving l.s. planes. The final cell constants were determined through global refinement of the xyz centroids of the reflections harvested from the entire data set. Structure solution and refinement were carried out using the SHELXTL-PLUS software package. Data (excluding structure factors) on the structures reported here had been deposited with the Cambridge Crystallographic Data Centre with deposition numbers. CCDC 1914539 contain the supplementary crystallographic data for this paper. These data could be obtained free of charge from The Cambridge Crystallographic Data Centre via www.ccdc.cam.ac.uk/data_request/cif.

3 | RESULTS AND DISCUSSION

The synthetic route for **TPE-Ca** is shown in Scheme 1. A Knoevenagel reaction between 4-(1,2,2-triphenylvinyl) benzaldehyde and 2-(4′-(8a,9a-dihydro-9H-carbazol-9-yl)-[1,1′-biphenyl]-4-yl)acetonitrile in ethanol led to the formation of **TPE-Ca** (70%). The target compound was fully characterized by ^{1}H/^{13}C NMR spectroscopy, single crystal X-ray diffraction, as well as by HRMS. **TPE-Ca** exhibits good solubility in common organic solvents, such as toluene, dichloromethane (DCM), tetrahydrofuran (THF), and 1,4-dioxane, but does not dissolve in water.

3.1 | X-ray single-crystal diffraction analysis

A single crystal of **TPE-Ca** (CCDC:1914539) was grown from a mixture of CH_2Cl_2 and hexane (1:1) at room

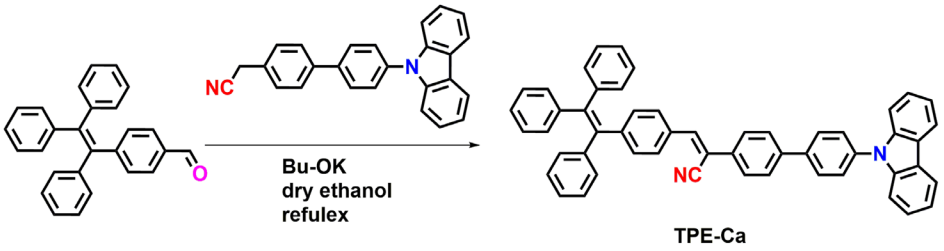

SCHEME 1 Synthetic route for **TPE-Ca**

TABLE 1 The photophysical and electrochemical properties of **TPE-Ca**

Compd.[a]	λ_{maxabs} (nm)	λ_{maxPL} (nm)	Φ_f	ι(ns)	$K_r(\times 10^{-8}\ s^{-1})$ (Φ_f/τ_f)	K_{nr} $(\times 10^{-8}\ s^{-1})$ $(1/\tau_f - k_r)$	LUMO (eV)	HOMO (eV)	△E (eV)
TPE-Ca	378 (THF)	505 (THF)	0.01	0. 5	0.2	19.8			
		515 (90%)	0.24	1.5	1.6	5.1	−2.48[b]	−5.58[b]	3.10[b]
	414 (film)	514 (99%)	0.36	2.17	1.7	2.9	−2.19[c]	−5.00[c]	2.81[d]
		504 (film)	0.6	1.7	3.5	2.4			

[a]Measured in THF and THF/water mixtures with different water fractions at room temperature.
[b]DFT/B3LYP/6-31G (d p)* using Gaussian 09.
[c]Values calculated using the ferrocene HOMO level by Cyclic Voltammetry using the empirical formulae HOMO = $-(4.8 + E_{onset}^{ox} - E_{onset[Fc]}^{ox})$.
[d]Calculated from λ_{edge}.

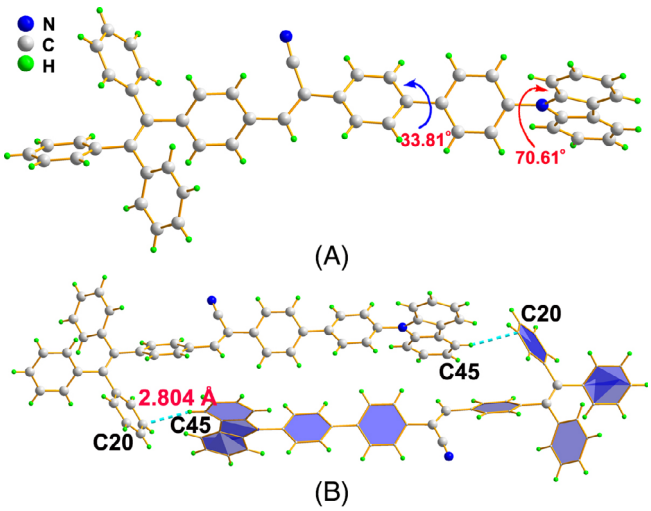

FIGURE 1 A, The X-ray structure of **TPE-Ca** and B, its crystal packing

temperature. The single-crystal X-ray structure of **TPE-Ca** adopts the monoclinic system with space group $P_1\ 2_1/n\ 1$. The key parameters are listed in Table 1. The molecule (Figure 1) adopts a twisted conformation with a large dihedral angle. The torsion angle between the terminal unit of the carbazole group and the phenyl ring is 70.61°. The molecular packing of **TPE-Ca** can best be described as off-set head-to-tail stacking. Each fragment of the molecule (such as the TPE and carbazole units) are linked to each other by several weak C-H···π interactions with distances in the range 2.28 to 2.80 Å. Generally, the non-planar conformation of **TPE-Ca** not only contributes to free intramolecular rotation in solution, but also to the formation of a close-packing matrix, which can inhibit intramolecular rotation and result in enhanced fluorescence efficiency. Indeed, the **TPE-Ca** molecule exhibits clear AIE characteristics.

3.2 | Photophysical properties

The PL spectra of **TPE-Ca** was measured in THF and in THF with different water fractions (f_w) (Figure 2). The **TPE-Ca** exhibited weak emission with a maximum emission peak at 505 nm in THF solution ($\Phi_F = 0.01$). On gradual addition of water to the THF from 0 to $f_w = 99\%$, the emission intensity of **TPE-Ca** enhanced *ca*. 100-fold with limited observed red-shifts (<10 nm) compared to the use of pure THF solution (Figure 2B) ($\Phi_F = 0.36$). Meanwhile, upon photoexcitation, **TPE-Ca** in the solid state displayed bright green emission at 502 nm with a narrow full width at half maxima (FWHM). The fluorescence quantum yield ($\Phi_{solid} = 0.6$) is higher than that both in solution (0.01) and in aggregated state (0.36). On the other hand, the radiative decay rate (k_r) of **TPE-Ca** increased from $2 \times 10^{-9}\ s^{-1}$ in solution to $3.5 \times 10^{-8}\ s^{-1}$ in the solid state, while the non-radiative decay rate constant (k_{nr}) decreased from $19.8 \times 10^{-8}\ s^{-1}$ to $2.4 \times 10^{-8}\ s^{-1}$, indicating that the molecular rotation was restricted by several

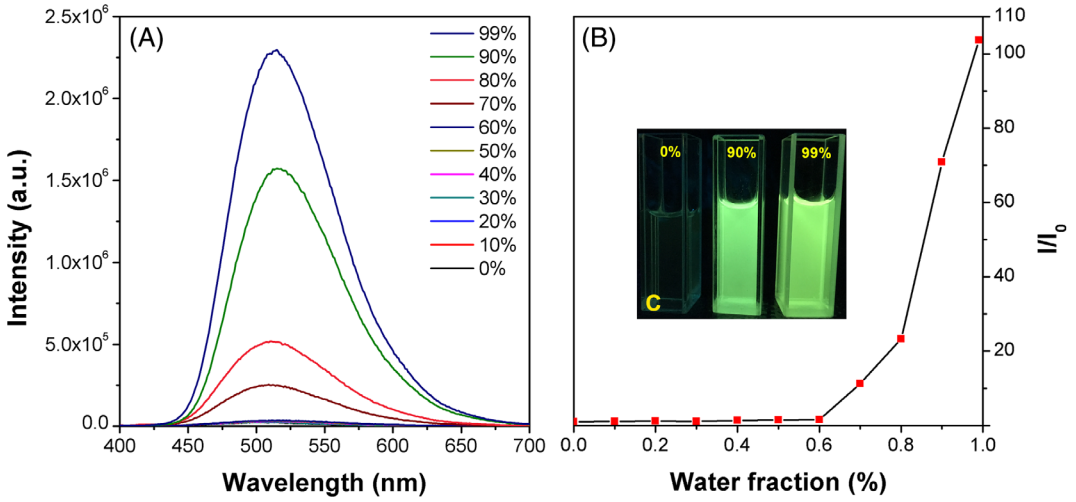

FIGURE 2 A, PL spectra of **TPE-Ca** in THF/water mixtures with different water fractions (f_w). B, Plot of relative PL intensity (I/I_0) *vs* the composition of THF/water mixture of **TPE-Ca**, where I_0 is the PL intensity in pure THF solution. C, Inset: fluorescent photographs of **TPE-Ca** in THF/ water mixtures (f_w = 0, 90% and 99%) taken under UV illumination (λ_{ex} = 365 nm)

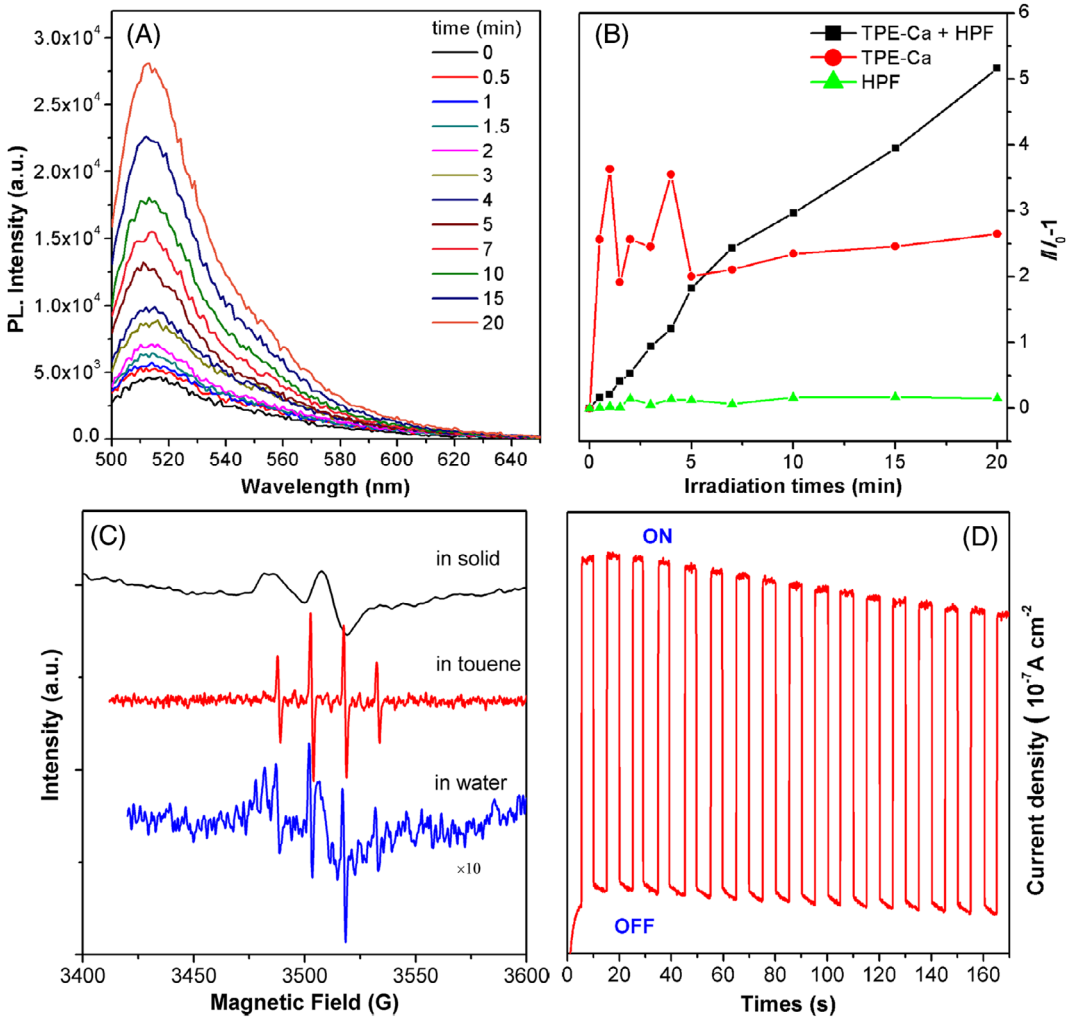

FIGURE 3 A, The fluorescence spectra of TPE with HPF in water under UV irradiation. B, The plot of I/I_0-1 values *vs* the irradiation time (solution concentration: 10^{-5} M). C, EPR spectra of **TPE-Ca** in the solid state, toluene and water, respectively. D, Transient photocurrent response of pure **TPE-Ca** photocatalysts electrodes with light on–off cycles [Na_2SO_4] = 0.1 M under solar light irradiation

weak C—H···π interactions, thereby blocking the non-radiative relaxation process[18] (Table 1).

3.3 | Radical detection

According to previous reports, many examples have illustrated that AIEgens can be utilized to monitor PDT, cell apoptosis, as well as the imaging of cell organelle by ROS generation under light irradiation, and these processes are closely reliant on the active radical.[19] Liu *et al.*[20] reported the relationship between the value of the lowest singlet excited state (S1), the lowest triplet excited state (T1) ($\Delta E_{S1\text{-}T1}$, ΔE_{ST}), and the efficiency to generate ROS by intersystem crossing (ISC); lower ΔE_{ST} values for AIEgens benefit the release of ROS. Thus, in the case of **TPE-Ca**, the optimized molecular geometry and the electron-density distribution of HOMO and LUMO were calculated using Gaussian 09 software at the B3LYP/6-31G (d, g) basis level (Table S2).[21] The calculated TD-DFT value for ΔE_{ST} is 0.26 eV, indicating that the **TPE-Ca** would be highly efficient for ROS generation and for the potential photodegradation of organic pollutants.

To investigate the formation of ROS from **TPE-Ca**, the generation of •OH species was further confirmed using the fluorescent probe, 4-hydroxyphenyl fluorescein (HPF),[22] which showed no emission, but fluoresced strongly after reacting with the •OH radical. As shown in Figure 3A,B, upon illumination of the mixture of **TPE-Ca** and HPF in water, the fluorescence was greatly enhanced with a positive linear relationship between the irradiation time and fluorescence intensity. Both results were consistent with the origin of the •OH signal being water in the presence of the **TPE-Ca** under irradiation.

More importantly, EPR spin-trap tests were performed for further confirming the •OH radical in the solid state and on a suspension. As depicted in Figure 3C, the EPR spectra of the solid sample **TPE-Ca** exhibited a strong EPR single with a g value of 2.002, which corresponds to the value for the free electron.[23] Irradiating the **TPE-Ca** over 5 minutes using DMPO as the Spin-trapping reagent, a clear EPR •OH signal with four well-resolved lines was detected centered at g = 2.006 in toluene, while two EPR signals were observed with g values of 2.008 and 2.015, respectively in water, due to the free electrons of **TPE-Ca** and •OH species. Thus, we assume that the origin of the •OH signal is from the H_2O generated in the presence of a radical of **TPE-Ca,** which would be further employed for the photocatalytic photodegradation of organic dyes.

Furthermore, to test the separation efficiency of the photo-generated electron-hole pairs, the current density *vs* time (I-t) characteristic was measured under a repeated ON/OFF AM 1.5 illumination (Figure 3D). The **TPE-Ca** exhibited a swift photo response with stable photocurrent density under visible light irradiation. In the absence of light irradiation (OFF), the photocurrent density rapidly dropped to almost zero, and the photocurrent reverted when the light was again ON. In addition, the current density decreased to *ca*. 10% under light irradiation after 20 cycles, which indicated that the **TPE-Ca** exhibited a reproducible photo-current with good photo-stability.

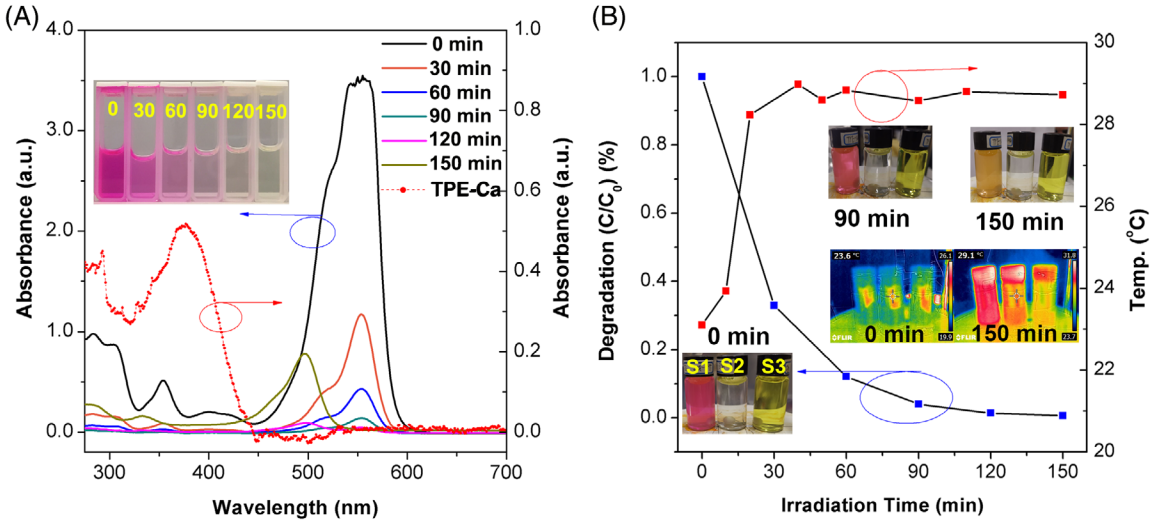

FIGURE 4 A, UV–vis spectra to monitor the process of photocatalytic degradation of RhB. B, Relative concentration (C/C_0) and temperature *vs* time plot for the photo-degradation of RhB in the presence of **TPE-Ca** in aqueous solution. Inset: thermal imaging of samples (from left to right: S1: **TPE-Ca**@RhB in water, S2: **TPE-Ca** in water and S3: **TPE-Ca** in THF)

3.4 | Photocatalytic activity

To evaluate the photocatalytic activity of **TPE-Ca**, the photo-degradation reaction was performed under visible light irradiation (simulated sunlight irradiation) in aqueous solution using rhodamine B (RhB) as the model organic pollutant. The adsorption equilibria of the mixture of **TPE-Ca (**5 mg**)** with RhB (10 mg/L) were obtained by stirring in the dark, and subsequently irradiating with simulated solar light. The photo-degradation behavior was then demonstrated by UV-vis spectra.

Generally, the RhB aqueous solutions remain stable under visible light irradiation over 180 minutes.[24] According to Figure 4A, the UV-vis curves indicate that the RhB was almost completely degraded with the extreme degradation ratio of 98.7% within 120 minutes in the presence of **TPE-Ca**, and the photodegradation efficiency of **TPE-Ca** was higher than that with common inorganic photocatalysts, such as C_3N_4,[5e] TiO_2,[25] as well as some heterogeneous systems.[26] When extending the irradiation time to 150 minutes, we observed that the suspension color changed from transparent to yellow-green, which may result from the formation of photocatalytic degradation products that accelerate the solubility of **TPE-Ca** in aqueous solution. Clearly, the **TPE-Ca** can play a significant role in the photo-degradation of RhB.

Meanwhile, thermal imaging technology was used to follow the entire photo-induced degradation process (Figure 4B). Interestingly, the change in temperature of the mixture **TPE-Ca**@RhB in water (S1) was remarkably different when compared to the **TPE-Ca** in water suspension (S2) and in THF (S3) solution when irradiated with sunlight. As Figure 4B shows, the temperature of **TPE-Ca** in water (S2) increased from 23.6°C to 29.1°C under light

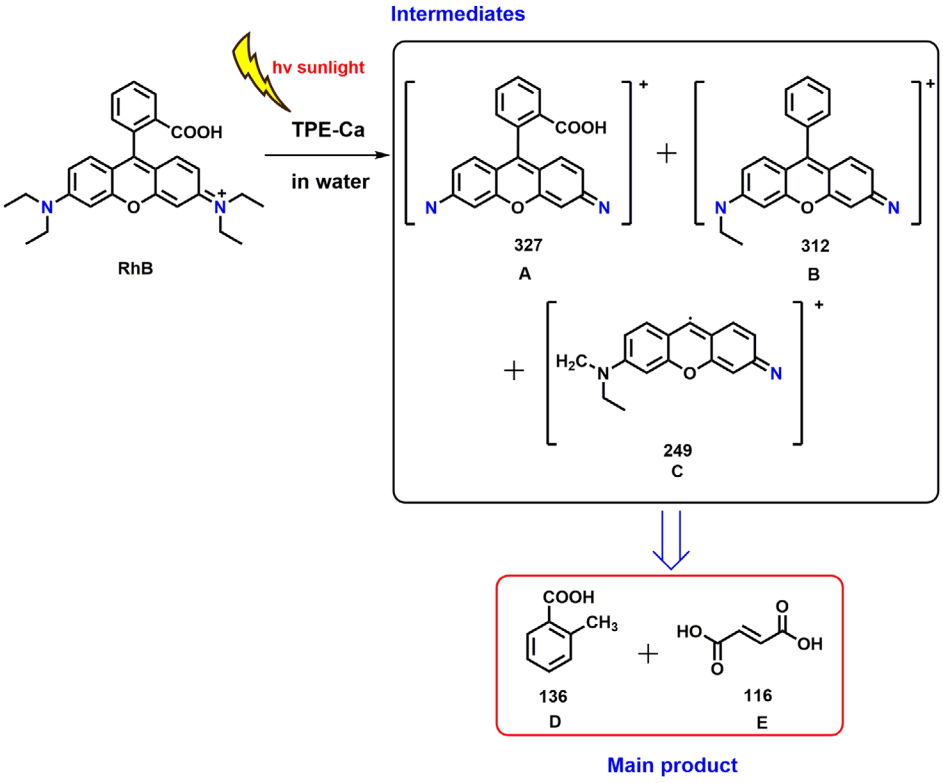

FIGURE 5 Possible final products of the photocatalytic degradation of RhB in the presence of **TPE-Ca**

TABLE 2 The high-resolution XPS spectrum of C1s, N1s and O1s peaks

Bond type	Peak BE	Bond type	Peak BE	Bond type	Peak BE
C-C	283.35	C-N	398.15	C-O	531.25
C-C	283.9	CN	399.11	C-O-C	532.54
C-N	284.95	Pyrrolic	401.71	N-O	533.5
CN	285.95	N^+	405.65	OH	534.7
C-O	288				
π-plasmon	290.77				

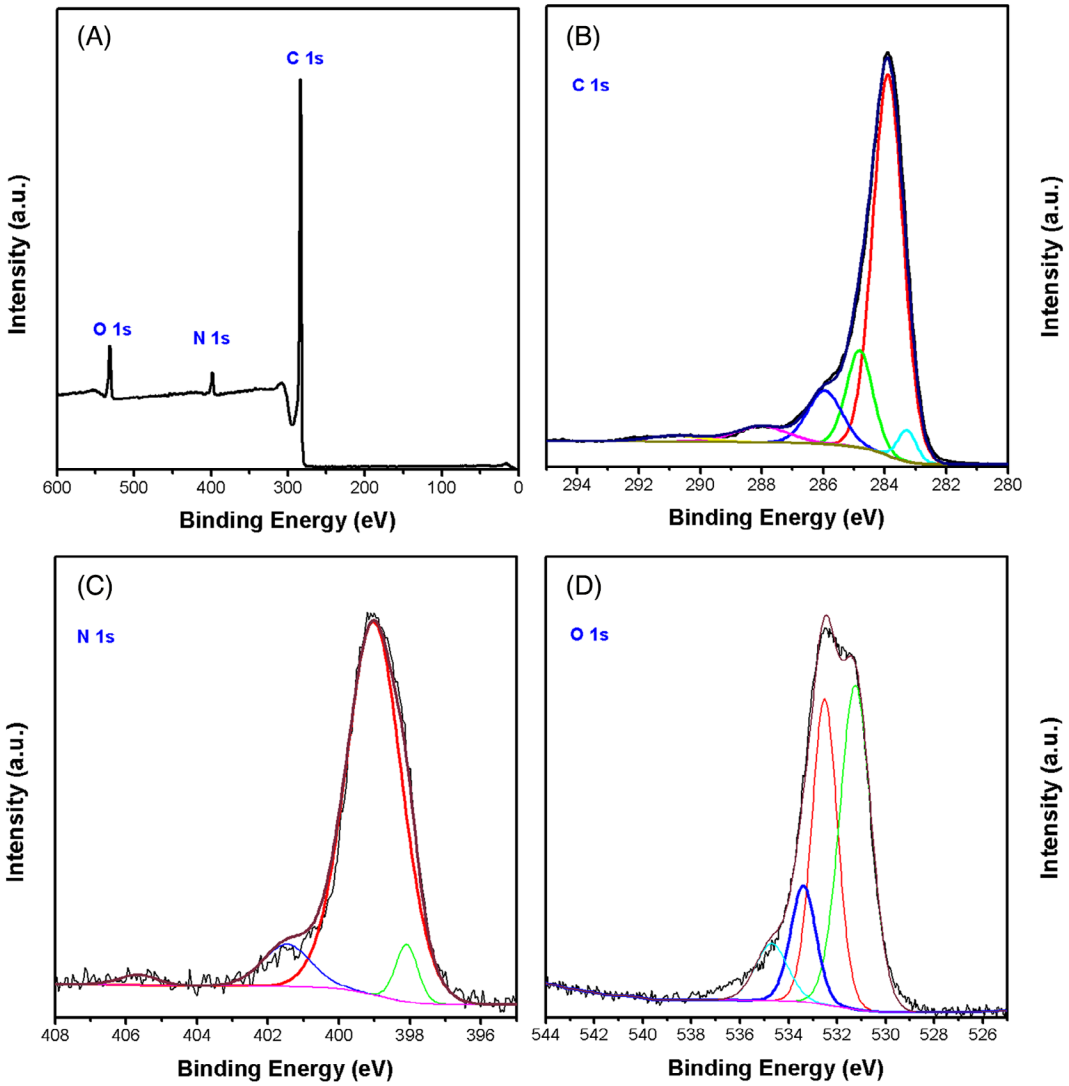

FIGURE 6 A, XPS spectrum of TPE-Ca, B, Carbon 1 second, C, Nitrogen 1 second and D, oxygen 1 second XPS spectra of **TPE-Ca**

irradiation for 150 minutes. More importantly, the temperature of S1 is higher than S2, which in turn is higher than S3.

In addition, the final products of the photocatalytic degradation of RhB were examined by UPLC/HDMS. The UPLC chromatograms retention time at 3.45 minutes was observed, which corresponds to the intermediates **A**-**E** (Figures S8-S13). The HDMS results indicate that the main intermediates consist of *N*-de-ethylated derivatives (**A**, **B**, and **C**), benzoic acid (**D**), and phthalic acid (**E**). Based on the UPLC/HDMS results, we propose a possible degradation pathway for RhB as listed in Figure 5. Firstly, after irradiation of **TPE-Ca** in water, RhB was degraded to radicals **A**, **B**, and **C**. These unstable intermediates subsequently degrade to the more stable, small molecules (**D** and **E**) under visible light irradiation.[27] The HLF and COS7 cells were incubated with final photocatalytic degradation product mixtures **1** (irradiation 120 minutes) and **2** (irradiation 150 minutes) in the medium for 1 hour at 37°C, and then were washed three times with phosphate-buffered saline solution (PBS, pH = 7.4) before imaging under a confocal fluorescence microscope. In Figures S15-S18, the confocal images of HLF and COS7 cells exhibit normal morphology with good health, and both final photo-degradation products **1** and **2** are found to rarely enter the cells. In addition, the cell viability results showed that both cells remain close to 100% (>90%) over 24 hours at a concentration of 0.6-3.0 g/mL, indicating the low cytotoxicity of the degradation compounds. Consistent with previous reports that Rhodamine B has moderate toxicity against normal cells and housefly,[28-30] our control experiments also show similar concentration-dependent toxicity (Figure S18A).[28-30] More importantly, after irradiation, the yellow residue was filtered and collected, then characterized by NMR spectroscopy. We observed the proton chemical shift is

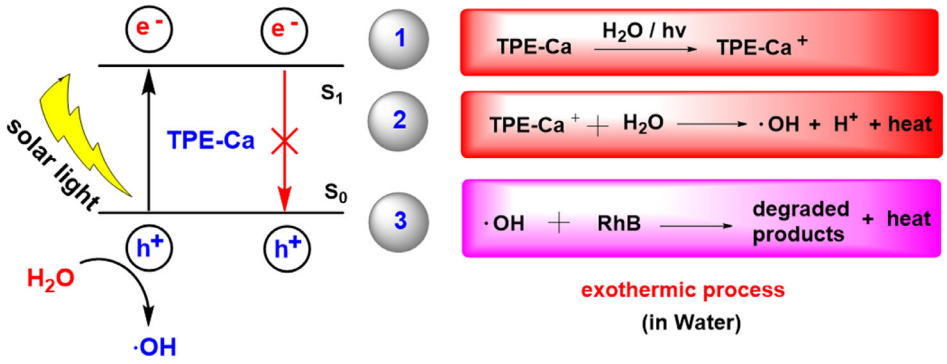

FIGURE 7 The possible photocatalytic process of **TPE-Ca**

almost the same as that in the original **TPE-Ca**, indicating that the photocatalyst has great stability (Figure S19).

3.5 | Photocatalytic mechanism

3.5.1 | XPS spectrum

XPS was preformed to analyze the electronic and chemical environment of the radicals and revealed the detailed elements that **TPE-Ca** is comprised of, *viz* C1s (283.88 eV), N1s (398.7 eV), and O1s (540 eV) the Auger lines carbon KL1 (1219 eV) and nitrogen KL2 (1139 eV) (Figures S20 and S21). As Figure 6 shows, the high-resolution XPS spectra of the C1s peaks can be divided into six peaks with binding energies at 283.35, 283.9, 284.95, 285.95, 288, 290.77 eV, which correspond to the C-C, C-C, C-N, C-N, C-O, and π-plasmon, respectively.[31] The N1s peak at 398.15, 399.11, 401.71, and 405.65 eV were assigned to C-N, C-N and the minor amount of oxidized N species (N-O• [401.71 eV] and $^{+}$N-O [405.65 eV]),[32] while the peaks at 531.25 and 532.54 eV for O 1 second were ascribed to C-O, C-O-C, and the peaks at 533.5 and 534.7 eV assigned to N-O radical and OH groups from adsorbed water, respectively (Table 2).[22,31] The above analysis indicated that the radical is intact, which is fully consistent with the EPR results in the solid state.

3.5.2 | Possible photocatalytic mechanism

In the absence of UV-irradiation, the mixture of **TPE-Ca** with RhB in water was stirred overnight and was then submitted for TEM measurements. As shown in Figure S24, the TEM images show that **TPE-Ca** exists as rounded nanoparticles with diameter of 7 to 10 nm, which disperse well in solution. More importantly, the high-order selected-area electron diffraction pattern suggests the nanoparticles of **TPE-Ca** still retain high quality crystallization.

Generally, AIEgens emit strong fluorescene in the aggregation state which is attributed to restricted intramolecular rotation (RIR) and restriction of intramolecular vibration (RIV), whereas molecular become more rigidity and block the non-radiative decay channels.[12] The emission intensity enhances in proportion to the morphologies and size of the nanoparticles, thus for more molecules aggregating, more nanoparticle homogeneity there is brighter emissive.[33] In this case, the small size of the AIEgens nanoparticle might annihilate the excitons through non-radiative decay pathways and produce radicals.

Thus, the observations from the TEM, EPR, and XPS results illustrated the possible photocatalytic process: (a) An electron is ejected from **TPE-Ca** under irradiation resulting in radical **TPE-Ca^{+}**, (b) the radical can react with water to generate a hydroxyl radical in an exothermic process by cleavage of the oxygen hydrogen bond, and (c) the hydroxyl radical plays a significant role in degrading the RhB to achieve the final products (Figure 7). On the other hand, for S1, under irradiation, an exothermic reaction occurs when the radical of **TPE-Ca** reacts with H_2O to produce •OH. Moreover, the •OH species involved in the oxidation reaction can generate enormous amounts of thermal energy, and S3 exhibited a relatively high temperature in comparison to S2, during the oxidation reactions indicating that the photo-degradation was rapid.[34,35]

4 | CONCLUSION

In summary, we have explored an efficient photo-degradation method for organic pollutants (RhB) by using a tetraphenylethene-based AIEgen (**TPE-Ca)** as a photocatalyst. UV-vis spectroscopic monitoring of the **TPE-Ca** system revealed enhanced photocatalytic ability toward photo-degradation of RhB which occurred with high efficiency (98.7%) under white light irradiation over

120 minutes. Importantly, both chemical and physical interactions generate enormous amounts of thermal energy and enhance the local environmental temperature. The identities of the final degradation products were confirmed by UPLC/HDMS, and these products displayed weak cytotoxicity toward HLF and COS7 cell lines. A photocatalytic mechanism was proposed on the basis of EPR and XPS results, which indicated that the **TPE-Ca** displayed a free electron signal, which would induce •OH for further photocatalytic processes. We report here the first example of an AIEgen as a high-performance photo-catalyst for environmental applications, and the use of thermal imaging technology for monitoring the photo-induced degradation process. This research opens up new avenues for the application of AIE research.

ACKNOWLEDGEMENTS

This work was supported by the National Natural Science Foundation of China (21975054, 51620105009, and 21602014), Natural Science Foundation of Guangdong Province of China (2019A1515010925), "One Hundred Talents Program" of the Guangdong University of Technology (GDUT) (1108-220413205). M. M. Islam thanks MOST, P. R. China for Talented Young Scientist Program (TYSP) Fellowship (402180111) and "The Pearl River Talent Recruitment Program"; CR thanks the EPSRC for an Overseas Travel Grant (EP/R023816/1). We also thank the technical support from AIEgen Biotech Co., Ltd.

CONFLICT OF INTEREST

The authors declare no competing financial interests.

REFERENCES

1. a) Vörösmarty CJ, McIntyre PB, Gessner MO, et al. Global threats to human water security and river biodiversity. *Nature*. 2010;467:555-561. b) Zhang H, Chen D, Lv X, Wang Y, Chang H, Li J. Energy-efficient photo-degradation of azo dyes with TiO_2 nanoparticles based on photo-isomerization and alternate UV-visible light. *Environ Sci Technol*. 2009;44:1107-1111.
2. a) Chong MN, Jin B, Chow CWK, Saint C. Recent developments in photocatalytic water treatment technology: a review. *Water Res*. 2010;44:2997-3027. b) Michael I, Rizzo L, McArdell CS, et al. Urban wastewater treatment plants as hotspots for the release of antibiotics in the environment: a review. *Water Res*. 2013;47:957-995.
3. a) Wenderich K, Mul G. Methods, mechanism, and applications of photo-deposition in photocatalysis: a review. *Chem Rev*. 2016;116:14587-14619. b)Kubacka A, Fernandez-Garcia M, Colon G. Advanced nano-architectures for solar photocatalytic applications. *Chem Rev*. 2011;112:1555-1614. c)Chen X, Shen S, Guo L, Mao SS. Semiconductor-based photocatalytic hydrogen generation. *Chem Rev*. 2010;110:6503-6570.
4. a) Yan J, Li P, Ji Y, Bian H, Li Y, Liu SF. Earth-abundant elements doping for robust and stable solar-driven water splitting by FeOOH. *J Mater Chem A*. 2017;5:21478-21485. b) Wang W, Dong J, Ye X, Li Y, Ma Y, Qi L. Heterostructured TiO_2 nanorod@ nanobowl arrays for efficient photo-electrochemical water splitting. *Small*. 2016;12:1469-1478. c) Zhang M, Mitchell RW, Huang H, Douthwaite RE. Ordered multilayer films of hollow sphere aluminium-doped zinc oxide for photo-electrochemical solar energy conversion. *J Mater Chem A*. 2017;5:22193-22198. d) Waiskopf N, Ben-Shahar Y, Galchenko M, et al. Photocatalytic reactive oxygen species formation by semiconductor–metal hybrid nanoparticles. Toward light-induced modulation of biological processes. *Nano Lett*. 2016;16:4266-4273.
5. a) Dhakshinamoorthy A, Asiri AM, Garcia H. Metal–organic framework (MOF) compounds: photocatalysts for redox reactions and solar fuel production. *Angew Chem Int Ed*. 2016;55:5414-5445. b) Qiu J, Zhang X, Feng Y, Zhang X, Wang H, Yao J. Modified metal-organic frameworks as photocatalysts. *Appl Catal B Environ*. 2018;231:317-342. c) Zhang B, Zhao SY, Wang HH, et al. The solution-phase process of a g-C_3N_4/$BiVO_4$ dyad to a large-area photoanode: interfacial synergy for highly efficient water oxidation. *Chem Commun*. 2017;53:10544-10547. d) Zhou M, Hou Z, Zhang L, Liu Y, Gao Q, Chen X. n/n junctioned g-C_3N_4 for enhanced photocatalytic H_2 generation. *Sustain Energ Fuels*. 2017;1:317-323. e) Liang Q, Li Z, Yu X, Huang ZH, Kang F, Yang QH. Macroscopic 3D porous graphitic carbon nitride monolith for enhanced photocatalytic hydrogen evolution. *Adv Mater*. 2015;27:4634-4639.
6. a) Sevim AM. Synthesis and characterization of Zn and Co monocarboxy-phthalocyanines and investigation of their photocatalytic efficiency as TiO_2 composites. *J Organomet Chem*. 2017;832:18-26. b) Tahir MB. Construction of MoS_2/CND-WO_3 ternary composite for photocatalytic hydrogen evolution. *J Inorg Organomet P*. 2018;28:2160-2168.
7. Routray S, Lenka TR. Polarization charges in a high-performance GaN/InGaNcore/shell multiple quantum well nanowire for solar energy harvesting. *IEEE T Nanotechnol*. 2018;17:1118-1124.
8. Liu X, Liu B, Li G, Liu Y. Two anthracene-based metal–organic frameworks for highly effective photodegradation and luminescent detection in water. *J Mater Chem A*. 2018;6:17177-17185.
9. Jia H, He W, Wamer WG, et al. Generation of reactive oxygen species, electrons/holes, and photocatalytic degradation of rhodamine B by photoexcited CdS and Ag_2S micro-nano structures. *J Phys Chem C*. 2014;118:21447-21456.
10. a) Zhu N, Wang S, Tang C, et al. Protection mechanisms of periphytic biofilm to photocatalytic nanoparticle exposure. *Environ Sci Technol*. 2019;53:1585-1594. b)Ahmad T, Farooq U, Phul R. Fabrication and photocatalytic applications of perovskite materials with special emphasis on alkali-metal-based niobates and tantalates. *Ind Eng Chem Res*. 2018;57:18-41. c) Zeng L, Guo X, He C, Duan C. Metal–organic frameworks: versatile materials for heterogeneous photocatalysis. *ACS Catal*. 2016;6:7935-7947. d) Montini T, Melchionna M, Monai M, Fornasiero P. Fundamentals and catalytic applications of CeO_2-based materials. *Chem Rev*. 2016;116:5987-6041. e) Jeon TH, Koo MS, Kim H, Choi W. Dual-functional photocatalytic and photo-electrocatalytic systems for energy-and resource-recovering water treatment. *ACS Catal*. 2018;8:11542-11563.
11. a) Zhao L, Lin YL, Kim H, Giebink NC, Rand BP. Donor/acceptor charge-transfer states at two-dimensional metal halide perovskite and organic semiconductor interfaces. *ACS*

Energy Lett. 2018;3:2708-2712. b) Rajeshwar K. Solar energy conversion and environmental remediation using inorganic semiconductor–liquid interfaces: the road traveled and the way forward. *J Phys Chem Lett*. 2011;2:1301-1309.

12. a) Luo J, Xie Z, Lam JW, et al. Aggregation-induced emission of 1-methyl-1, 2, 3, 4, 5-pentaphenylsilole. *Chem Commun*. 2001;18:1740-1741. b) Hong Y, Lam JW, Tang BZ. Aggregation-induced emission. *Chem Soc Rev*. 2011;40:5361-5388. c) Mei J, Leung NL, Kwok RT, Lam JW, Tang BZ. Aggregation-induced emission: together we shine, united we soar! *Chem Rev*. 2015; 115:11718-11940. d) Qureshi WA. Current and future applications of the capsule camera. *Nat Rev Drug Discov*. 2004;3:447-450. e Islam MM, Hu Z, Wang Q, Redshaw C, Feng X. Pyrene-based aggregation-induced emission luminogens and their applications. *Mater Chem Front*. 2019;3:762-781.
13. a Zhu H, Goswami N, Yao Q, et al. Cyclodextrin–gold nanocluster decorated TiO_2 enhances photocatalytic decomposition of organic pollutants. *J Mater Chem A*. 2018;6:1102-1108. b Chen J, Dong CL, Zhao D, et al. Molecular design of polymer heterojunctions for efficient solar–hydrogen conversion. *Adv Mater*. 2017;29:1606198.
14. a) Xu S, Wu W, Cai X, et al. Highly efficient photosensitizers with aggregation-induced emission characteristics obtained through precise molecular design. *Chem Commun*. 2017;53: 8727-8730. b) Zhu C, Kwok RT, Lam JW, Tang BZ. Aggregation-induced emission: a trailblazing journey to the field of biomedicine. *ACS Appl Bio Mater*. 2018;1:1768-1786. c) Zhuang Z, Dai J, Yu M, Li J, Shen P, Hu R. Type I photosensitizers based on phosphindole oxide for photodynamic therapy: apoptosis and autophagy induced by endoplasmic reticulum stress. *Chem Sci*. 2020;11:3405-3417.
15. Wei P, Zhang JX, Zhao Z, et al. Multiple yet controllable photoswitching in a single AIEgen system. *J Am Chem Soc*. 2018;140:1966-1975.
16. a) Zhao N, Li P, Zhuang J, et al. Aggregation-induced emission luminogens with the capability of wide color tuning, mitochondrial and bacterial imaging, photodynamic anticancer and antibacterial therapy. *ACS Appl Mater Interfaces*. 2019;11:11227-11237. b) Chen M, Li L, Nie H, et al. Tetraphenylpyrazine-based AIEgens: facile preparation and tunable light emission. *Chem Sci*. 2015;6:1932-1937. c) Chen M, Chen R, Shi Y, et al. Malonitrile-functionalized tetraphenylpyrazine: aggregation-induced emission, ratiometric detection of hydrogen sulfide, and mechanochromism. *Adv Funct Mater*. 2018;28:1704689.
17. a) An BK, Gierschner J, Park SY. π-Conjugated cyanostilbene derivatives: a unique self-assembly motif for molecular nanostructures with enhanced emission and transport. *Acc Chem Res*. 2011;45:544-554. b) Kokado K, Sada K. Consideration of molecular structure in the excited state to design new organic luminogens with aggregation-induced emission. *Angew Chem Int Ed*. 2019;58:8632-8639. c) Zhang H, Zheng X, Xie N, et al. Why do simple molecules with "isolated" phenyl rings emit visible light? *J Am Chem Soc*. 2017;139:16264-16272.
18. a) Sekiguchi S, Kondo K, Sei Y, Akita M, Yoshizawa M. Engineering atacks of V-shaped polyaromatic compounds with alkyl chains for enhanced emission in the solid state. *Angew Chem Int Ed*. 2016;55:6906-6910. b) Hong Y, Dong Y, Tong H, et al. Aggregation-and crystallization-induced light emission [C]//organic photonic materials and devices IX. *Int Soc Opt Photon*. 2007;6470:64700T. c) Wang J, Gu X, Zhang P, et al. Ionization and anion– π^+ interaction: a new strategy for structural design of aggregation-induced emission luminogens. *J Am Chem Soc*. 2017;139:16974-16979.
19. a) Zheng Z, Zhang T, Liu H, et al. Bright near-infrared aggregation-induced emission luminogens with strong two-photon absorption, excellent organelle specificity, and efficient photodynamic therapy potential. *ACS Nano*. 2018;12:8145-8159. b) Shi J, Li Y, Li Q, Li Z. Enzyme-responsive bioprobes based on the mechanism of aggregation-induced emission. *ACS Appl Mater Interfaces*. 2017;10:12278-12294. c) Mei J, Huang Y, Tian H. Progress and trends in AIE-based bioprobes: a brief overview. *ACS Appl Mater Interfaces*. 2018;10:12217-12261. d) Chen S, Li Q, Wang X, Yang YW, Gao H. Multifunctional bacterial imaging and therapy systems. *J Mater Chem B*. 2018;6: 5198-5214. e) Wu F, Wu X, Dua Z, Huang Y, Lou X, Xia F. Biomacromolecule-functionalized AIEgens for advanced biomedical studies. *Small*. 2019;15:1804839. f) Li X, Kim J, Yoon J, Chen X. Cancer-associated, stimuli-driven, turn on theranostics for multimodality imaging and therapy. *Adv Mater*. 2017;29: 1606857. g) Qi J, Chen C, Ding D, Tang BZ. Aggregation-induced emission luminogens: union is strength, gathering illuminates healthcare. *Adv Healthc Mater*. 2018;7:1800477.
20. a) Xu S, Yuan Y, Cai X, et al. Tuning the singlet-triplet energy gap: a unique approach to efficient photosensitizers with aggregation-induced emission (AIE) characteristics. *Chem Sci*. 2015; 6:5824-5830.
21. Frisch MJ, Trucks GW, Schlegel HB, Scuseria GE, Robb MA, Cheeseman JR. *Gaussian 09, Revision A.02*. Wallingford, CT: Gaussian, Inc.; 2009.
22. a) Li MD, Wong NK, Xiao J, et al. Dynamics of oxygen-independent photocleavage of blebbistatin as a one-photon blue or two-photon near-infrared light-gated hydroxyl radical photocage. *J Am Chem Soc*. 2018;140:15957-15968. b) Garcia-Diaz M, Huang YY, Hamblin MR. Use of fluorescent probes for ROS to tease apart type I and type II photochemical pathways in photodynamic therapy. *Methods*. 2016;109:158-166. c) Fitch KR, Goodwin AP. Mechanochemical reaction cascade for sensitive detection of covalent bond breakage in hydrogels. *Chem Mater*. 2014;26:6771-6776.
23. Gerson F, WILEY J, Huber W. *Electron Spin Resonance Spectroscopy of Organic Radicals*. Weinheim, Germany: WILEY-VCH Verlag GmbH & Co. KGaA; 2003.
24. Tonda S, Kumar S, Kandula S, Shanker V. Fe-doped and-mediated graphitic carbon nitride nanosheets for enhanced photocatalytic performance under natural sunlight. *J Mater Chem A*. 2014;2:6772-6780.
25. Zhao Z, Liu G, Li B, et al. Dye-sensitized solar cells based on hierarchically structured porous TiO_2 filled with nanoparticles. *J Mater Chem A*. 2015;3:11320-11329.
26. Maeda K, Domen K. Water oxidation using a particulate $BaZrO_3$-$BaTaO_2N$ solid-solution photocatalyst that operates under a wide range of visible light. *Angew Chem Int Ed*. 2012; 51:9865-9869.
27. Xu T, Wang D, Dong L, Shen H, Lu W, Chen W. Graphitic carbon nitride co-modified by zinc phthalocyanine and graphene quantum dots for the efficient photocatalytic degradation of refractory contaminants. *Appl Catal B Environ*. 2019;244: 96-106.

28. Ogawa T, Fujii H, Kawai K, Yatome C, Idaka E. Growth inhibition of bacillus subtilis upon interaction between basic dyes and DNA. *Bull Environ Contam Toxicol*. 1989;42:402-408.
29. Respicio NC, Heitz JR. Comparative toxicity of rhodamine B and rhodamine6G to the house fly (*Musca domestica* L.). *Bull Environ Contam Toxicol*. 1981;27:274-281.
30. Mahlambi MM, Mishra AK, Mishra SB, Krause RW, Mamba BB, Raichur AM. Effect of metal ions (Ag, Co, Ni, and Pd) on the visible light degradation of rhodamine B by carbon-covered alumina-supported TiO_2 in aqueous solutions. *Ind Eng Chem Res*. 2013;52:1783-1794.
31. a Chen G, Wang X, Li J, Hou W, Zhou Y, Wang J. Direct carbonization of cyanopyridinium crystalline dicationic salts into nitrogen-enriched ultra-microporous carbons toward excellent CO_2 adsorption. *ACS Appl Mater Interfaces*. 2015;7:18508-18518. b Ciccullo F, Gallagher NM, Geladari O, Chasse T, Rajca A, Casu MB. A derivative of the blatter radical as a potential metal-free magnet for stable thin films and interfaces. *ACS Appl Mater Interfaces*. 2016;8:1805-1812. c Zhao S, Lan M, Zhu X, et al. Green synthesis of bifunctional fluorescent carbon dots from garlic for cellular imaging and free radical scavenging. *ACS Appl Mater Interfaces*. 2015;7:17054-17060. d Moulder JF. *Handbook of X-Ray Photoelectron Spectroscopy*. Physical Electronics; 1995:230-232.
32. a Gadgil B, Damlin P, Viinikanoja A, Heinonen M, Kvarnström C. One-pot synthesis of an Au/Au_2S viologen hybrid nanocomposite for efficient catalytic applications. *J Mater Chem A*. 2015;3:9731-9737. b Lin Y, Su D. Fabrication of nitrogen-modified annealed nanodiamond with improved catalytic activity. *ACS Nano*. 2014;8:7823-7833. c Yang P, Wang R, Zhou M, Wang X. Photochemical construction of carbonitride structures for red-light redox catalysis. *Angew Chem Int Ed*. 2018;57:8674-8677. d Low JZ, Kladnik G, Patera LL, et al. The environment-dependent behavior of the blatter radical at the metal-molecule interface. *Nano Lett*. 2019;19:2543-2548. e Flavin K, Lawrence K, Bartelmess J, et al. Synthesis and characterization of boron azadipyrromethene single-wall carbon nanotube electron donor-acceptor conjugates. *ACS Nano*. 2011;5:1198-1206.
33. Feng X, Zhang J, Hu Z, et al. Pyrene-based aggregation-induced emission luminogens (AIEgen): structure correlated with particle size distribution and mechanochromism. *J Mater Chem C*. 2019;7:6932-6940.
34. Wang H, Guo H, Zhang N, Chen Z, Hu B, Wang X. Enhanced photo-reduction of U(VI) on C_3N_4 by Cr(VI) and bisphenol, A: ESR, XPS, and EXAFS investigation. *Environ Sci Technol*. 2019;53:6454-6461.
35. Zhang S, Song S, Gu P, et al. Visible-light-driven activation of persulfate over cyano and hydroxyl group co-modified mesoporous g-C3N4 for boosting bisphenol A degradation. *J Mater Chem A*. 2019;7:5552-5560.

SUPPORTING INFORMATION

Additional supporting information may be found online in the Supporting Information section at the end of this article.

How to cite this article: Hu Z, Li Y, Kang M, et al. Aggregation-induced emission luminogen: A new perspective in the photo-degradation of organic pollutants. *EcoMat*. 2020;1–12. https://doi.org/10.1002/eom2.12024